

Clumpy and fractal shocks, and the generation of a velocity dispersion in molecular clouds

C. L. Dobbs^{1,2*} and I. A. Bonnell¹¹*School of Physics and Astronomy, University of St Andrews, North Haugh, St Andrews, Fife, KY16 9SS*²*School of Physics, University of Exeter, Stocker Road, EX4 4QL*

11 October 2018

ABSTRACT

We present an alternative explanation for the nature of turbulence in molecular clouds. Often associated with classical models of turbulence, we instead interpret the observed gas dynamics as random motions, induced when clumpy gas is subject to a shock. From simulations of shocks, we show that a supersonic velocity dispersion occurs in the shocked gas provided the initial distribution of gas is sufficiently non-uniform. We investigate the velocity size-scale relation $\sigma \propto r^\alpha$ for simulations of clumpy and fractal gas, and show that clumpy shocks can produce realistic velocity size-scale relations with mean $\alpha \sim 0.5$. For a fractal distribution, with a fractal dimension of 2.2 similar to what is observed in the ISM, we find $\sigma \propto r^{0.4}$. The form of the velocity size-scale relation can be understood as due to mass loading, i.e. the post-shock velocity of the gas is determined by the amount of mass encountered as the gas enters the shock. We support this hypothesis with analytical calculations of the velocity dispersion relation for different initial distributions. A prediction of this model is that the line-of sight velocity dispersion should depend on the angle at which the shocked gas is viewed.

Key words: hydrodynamics – turbulence – ISM: clouds – ISM: kinematics and dynamics

1 INTRODUCTION

Molecular clouds are known to exhibit supersonic chaotic dynamics (Heyer & Brunt 2004; Ossenkopf & Mac Low 2002; Falgarone & Phillips 1990; Perault et al. 1985; Hayashi et al. 1989; Larson 1981), which are thought to control star formation and determine the properties of protostellar cores (Mac Low & Klessen 2004). Although referred to as ‘turbulence’, the origin and nature of these motions are not fully understood. The most general definition of ISM turbulence is simply that the gas exhibits random motions on many scales (Mac Low & Klessen 2004). However there is a consistent correlation observed in molecular clouds between the velocity dispersion and size scale (the Larson (1981) relation), approximately $\sigma \propto r^{0.5}$ (e.g. Myers (1983); Solomon et al. (1987); Brunt (2003)). This has invoked many comparisons between interstellar turbulence and classical turbulence, e.g. Kolmogorov incompressible turbulence (Passot et al. 1988; Falgarone & Phillips 1990) ($\sigma \propto L^{0.33}$); Burger’s shock dominated turbulence (Scalo et al. 1998) ($\sigma \propto L^{0.5}$); and the She-Leveque model for incompressible turbu-

lence (She & Leveque 1994; Boldyrev 2002) ($\sigma \propto L^{0.42}$ (Boldyrev et al. 2002)).

The possible sources of turbulence can be summarised as follows: gravitational, magnetic or hydromagnetic instabilities; galactic rotation, through magneto-rotational instabilities, shocks in spiral arms or collisions of clouds on different epicyclic orbits; stellar feedback via supernovae, stellar winds and HII regions. Recent simulations have indicated that turbulence induced by a large scale driving force (e.g. large scale flows from supernovae or galactic rotation) is more consistent with observed molecular cloud structures (Brunt 2003; Klessen 2001). Supernovae have been shown to produce sufficient energy to generate the velocity dispersions observed (Mac Low & Klessen 2004). However observations of turbulent velocities in regions which do not contain massive star formation suggests that other mechanisms, such as magneto-rotational instabilities (Piontek & Ostriker 2005; Sellwood & Balbus 1999) and colliding flows (Ballesteros-Paredes et al. 1999) must also be important. Interestingly, recent observations have suggested that the elongations of molecular clouds are more compatible with galactic rotation models rather than stellar feedback (Koda et al. 2006).

* E-mail: dobbs@astro.ex.ac.uk

Galactic disk simulations have investigated gravity

driven turbulence (Wada et al. 2002), stellar feedback (Wada & Norman 2001; de Avillez & Breitschwerdt 2005; Dib et al. 2006) and the influence of spiral density waves on ISM dynamics (Dobbs et al. 2006). Analytical results also indicate that vorticity is generated in centrally condensed clouds subject to galactic shocks (Kornreich & Scalo 2000), and the induced velocities follow the observed velocity size-scale relation. Previous numerical work on colliding flows showed that density and velocity perturbations occur even in uniform flows subject to cooling instabilities (Heitsch et al. 2005), although a velocity length scale correlation was not investigated. Simulations of clumpy flows have also indicated that a Salpeter type clump mass spectrum can be reproduced (Clark & Bonnell 2006).

Spiral shocks have also been proposed to explain the dynamics of molecular clouds (Bonnell et al. 2006; Zhang et al. 2001). Bonnell et al. (2006) model giant molecular cloud formation as gas passes through a clumpy spiral shock. The dynamics of the molecular clouds are determined on all scales simultaneously as the clouds form and the induced velocity dispersion size scale relation is consistent with observations. This can account for the observed velocity dispersions that are found even in regions devoid of massive stars. Furthermore, there is no need for a continuous driving mechanism as the time for the decay of these velocities is proposed to be of similar magnitude to the cloud lifetime.

In this paper we investigate the velocity size relation in shock tests with uniform, clumpy and fractal distributions of isothermal gas. The clumpy and fractal distributions are chosen to reflect the highly structured nature of the ISM (Cox 2005; Elmegreen & Scalo 2004; Dickey & Lockman 1990; Perault et al. 1985). We concentrate on modelling the passage of gas through a spiral arm by using a linear sinusoidal potential, although these results would apply generally to shocks between colliding flows. We show that random velocities induced in non-uniform shocks display a velocity size relation similar to those observed and provide simple analytical analysis alongside the results of our simulations. Thus the ‘turbulence’ in our results describes random motions of the gas and does not correspond to any theories of classical turbulence.

2 CALCULATIONS

We use the 3D smoothed particle hydrodynamics (SPH) code based on the version by Benz (Benz 1990). The smoothing length is allowed to vary with space and time, with the constraint that the typical number of neighbours for each particle is kept near $N_{neigh} \sim 50$. Artificial viscosity is included with either the standard parameters $\alpha = 1$ and $\beta = 2$ (Monaghan & Lattanzio 1985; Monaghan 1992) or $\alpha = 2$ and $\beta = 4$.

2.1 Initial conditions

We investigate uniform, clumpy and multi-scale shocks, starting with 3D shock tube tests first before considering gas subject to an external potential. In all calculations, the gas is isothermal, non self-gravitating and there are no magnetic fields. These calculations are dimensionless, and are

Test	Distribution	L	F (%)	\mathcal{M}
ST	Uniform	4	100	10
ST	Clumps ($r_{cl}=0.1$)	4	27	20
ST	Clumps ($r_{cl}=0.2$)	4	50	20
ST	Uniform	4	100	20
ST	Clumps ($r_{cl}=0.1$)	4	27	40
ST	Clumps ($r_{cl}=0.2$)	4	50	40
SP	Uniform	3	100	30
SP	Clumps ($r_{cl}=0.1$)	3	12	30
SP	Clumps ($r_{cl}=0.2$)	3	23	30
SP	Clumps ($r_{cl}=0.4, 0.1, 0.04$)	3	32	30
SP	2.2 D Fractal	3	10	30
SP	2.7 D Fractal	3	23	30

Table 1. Table showing the different runs performed and the distributions of gas used for initial conditions. ST and SP refer to shock tube and sinusoidal potential tests, L is the maximum initial length scale, F the volume filling factor and \mathcal{M} the Mach number of the shock. All simulations used 2×10^5 particles except for the fractal distributions which required either 2×10^6 or 3×10^6 particles.

characterized by the Mach number of the shock and the initial density distribution of the gas. In all calculations, the particles are allocated velocities in the x direction only and, except for the oblique shocks (Section 3.2), the gas shocks in the yz plane.

The parameters used in the different simulations are shown in Table 1. We investigated 4 distributions of gas - uniform, homogeneous spherical clumps in pressure equilibrium, spherical clumps of different radii/density and fractal distributions. The filling factors for each distribution are calculated by overlaying a 3D grid on each distribution and determining the porosity. The filling factor is given by $F = N_{full}/N_{total}$ where N_{full} is the number of cells containing at least 1 particle and N_{total} the total number of cells. We take a 32^3 grid, so the mesh resolution is equivalent to a couple of smoothing lengths for the uniform case. This ensures that each cell contains at least 1 particle for the uniform distribution so the filling factor is 100%. The maximum initial scale length corresponds to the range of x values for the particles in the initial distribution.

2.1.1 Shock tube test

We first perform 3D shock tube tests with initial distributions of uniform and clumpy gas to model colliding flows. For both distributions, particles are placed within a cuboid of dimensions $-2 < x < 2$, $-1 < y < 1$ and $-1 < z < 1$. To produce a clumpy shock we distribute the particles in uniform density spheres within these length scales. The clumps are a constant temperature, confined by either an external pressure field or a hotter diffuse phase. The clumps are initially allowed to settle into equilibrium before the simulation is carried out. To produce clumps of different radii, the external pressure (or pressure of the diffuse phase) can be increased or decreased. We then assign particles a velocity of $v_0 = 10 c_s$ for $x \leq 0$ and $v_0 = -10 c_s$ for $x > 0$. For the uniform distribution, this produces two approximately Mach 10 shocks, and multiple shocks of up to Mach 20 for the clumpy distributions. These calculations were also repeated

using twice the initial velocities and all tests use 2×10^5 particles.

2.1.2 Sinusoidal potential

We mainly consider shocks in gas subject to an external potential. In this case the gas self shocks, similar to gas experiencing a stellar potential in a spiral galaxy. A velocity dispersion relation similar to the observed $\sigma \propto r^{0.5}$ law has been shown to develop as gas passes through a clumpy spiral shock (Bonnell et al. 2006). Here we examine a simplified setup, where we can investigate the effect of the shock dynamics on the initial gas distribution. Instead of the spiral potential we use a 1D sinusoidal potential of the form

$$\psi = A \cos(k(x + B)). \quad (1)$$

where k is the wavenumber and B a length parameter to determine the location of the minimum. This is equivalent to the linear passage of gas through sinusoidal spiral arms. The dimensionless velocity acquired by gas falling from the peak to the base of the potential is $V_{pot} = \sqrt{2 \times A}$. We tried many different potentials, varying A and k , and only applying the potential once the gas has passed a minimum. However we found that the results presented here are largely independent of the exact nature of the potential. The structure of the shock is similar for different potentials for a given initial distribution. The relative strength of the shock determines the magnitude of the velocity dispersion, whilst the initial distribution determines the velocity size scaling law. For the simulations presented here, we took $k = \pi/4$, $A = 100$ and $B = 2$ to produce a minimum at 2 and maxima at -2 and 6.

We allocate particles a velocity of $50 c_s$ in the x direction and zero velocity in the y and z directions, which for the simulations described here, leads to a shock of Mach number ≈ 30 . We set up a distribution of spherical clumps in pressure equilibrium in the same way as described for the shock tube tests. Where a hot diffuse phase is used to supply an external pressure, the hot phase is distributed with the same number of particles (2×10^5), but $1/10$ of the mass of the cold phase.

We also test a distribution with clumps of different size-scales and densities, giving structure on a range of scales. The clumps have initial diameters of 0.4, 0.1 and 0.04, with clumps of smaller diameter placed inside larger clumps. For the uniform and clumpy distributions, particles are positioned within a cuboid of dimensions $-1.5 < x < 1.5$, $-1 < y < 1$ and $-1 < z < 1$. We also investigate shocks with an initial fractal distribution, following the method described in Elmegreen (1997) to generate fractals. The algorithm includes 3 parameters, an intrinsic length scale L , the number of hierarchical levels, H , and the number of points in each level, N . The dimension of the fractal is $D = \log N / \log L$ and the number of points is N^H . We generate a 2.2 D fractal, with $L = 2.1$, $N = 5$ and $H = 9$ requiring ≈ 2 million points, and a 2.7 D fractal, with $L = 2.5$, $N = 12$ and $H = 6$ requiring ≈ 3 million points. We then scale the x, y, z coordinates (equally) of each fractal to fit inside a cube of dimensions $-1.5 < x < 1.5$, $-1.5 < y < 1.5$ and $-1.5 < z < 1.5$. Observations estimate the interstellar fractal dimension as $D=2.3$ (Elmegreen & Falgarone 1996).

Since for the distributions with fractals or different

size clumps the gas exhibits different densities and pressures, constant pressure boundaries, or an intervening diffuse phase, are no longer appropriate. Instead we apply a pressure switch in order that only gas in the shocked region is subject to pressure forces. The gas experiences pressure only when $\text{div}(v) \leq 0$ i.e. compression of the gas is occurring. This enables structure on all scales to be maintained in the gas distribution before gas reaches the shock. Tests for the uniform density clumps showed this method produced similar results compared to when constant pressure boundaries were applied.

3 RESULTS

Column density plots for different simulations are shown in Fig. 1,2,3 (all for the sinusoidal potential tests). The uniform shock in Fig. 1 shows a smooth shocked region of approximately constant density and width. By contrast the clumpy shock (Fig. 1, middle) shows a much broader shocked region of non-uniform density. The shock contains more structure and appears more similar to simulations of turbulence. In Fig. 1 (middle), an external pressure field is applied to maintain the clumps in pressure equilibrium. Fig. 1 (lower) shows a shock for similar size clumps, where the clumps are instead surrounded by hotter gas. In this case, the hot gas takes the same numbers of particles as the cold gas, but $1/10$ of the mass. The ratio of the densities of cold to hot gas is ~ 30 , which is similar to the ratio of densities of the cold and warm neutral components of the ISM (Cox 2005). The structure of the cold gas in the shock is very similar whether the clumps are in equilibrium from external pressure boundaries, or hot gas, indicating that the hot gas has little effect on the gas dynamics.

The distribution of different size clumps shows similar morphology, although more smaller scale structure is apparent in the shocked gas (Fig. 2). The shocked gas of the fractal distribution (Fig. 3) shows more filamentary structure compared to the clumpy distributions.

3.1 Velocity dispersion

We now calculate the 1D velocity dispersion of the post-shock gas. We only consider the v_x velocities, which corresponds to the direction of motion of the initial gas, since the velocity dispersion in the y and z directions are always subsonic. For a given size, we average the velocity dispersion over numerous regions of that size scale. The regions are 3 D and chosen to centre on the densest particles in the shock. Only particles with densities greater than the maximum pre-shock density are considered for calculating the velocity dispersion, thus ensuring we only include gas in the shock. (We find that even for a uniform shock, including the pre and/or post shock gas will produce a Larson type velocity dispersion size-scale relation, theoretically and from numerical results.) We repeat this process for regions of different size-scale to determine the dependence of the induced velocity dispersion on the size-scale.

For the shock tube tests, we initially found that the velocity dispersion was supersonic, even for the uniform shock. This is due to the inherently clumpy nature of SPH which introduces error when calculating the velocity dispersion. We

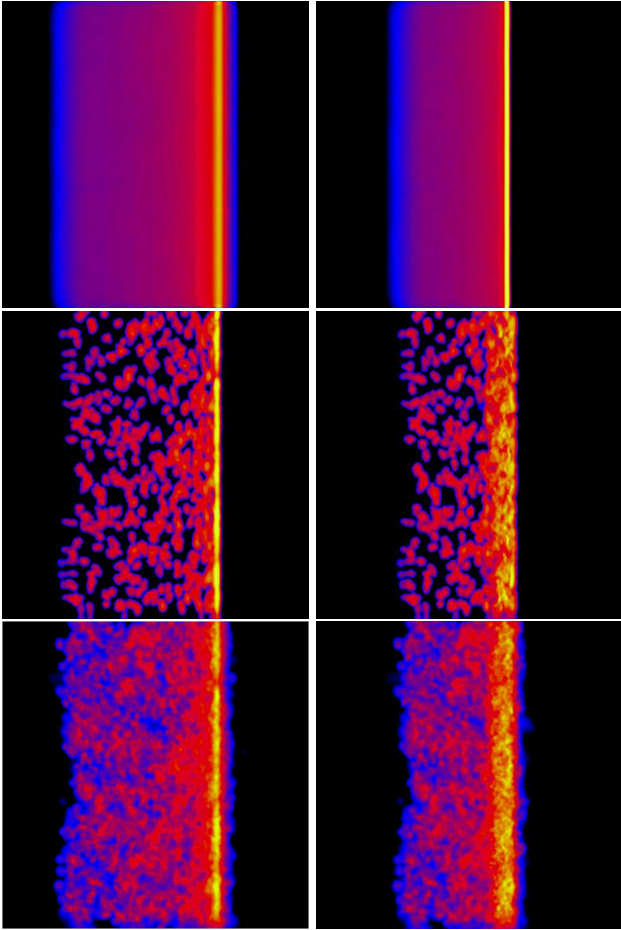


Figure 1. The column density distribution is shown for linear shock tests where gas is passed through a sinusoidal potential. The initial distribution is uniform (top) and clumpy (middle, bottom, where the clump radius is 0.1). The middle panels show the case where the clumps are confined by constant pressure boundaries, whereas for the bottom panels, the clumps are in equilibrium with a diffuse phase of gas. The left panels ($2.8 < x < 4.8$, $-1 < y < 1$) show the gas as it begins to shock ($t=0.15$) while the right panels ($3.2 < x < 5.2$, $-1 < y < 1$) show the gas when the shock is fully developed ($t=0.25$). The minimum and maximum of the potential lie at $x = 2$ and $x = 6$ respectively. The column density ranges from 90 to 9×10^6 in units of particles per unit area and the colour scale is logarithmic.

therefore increased the viscosity parameters to $\alpha = 2$ and $\beta = 4$. This lowered the values of the velocity dispersion for both the uniform Mach 10 and Mach 20 shocks, although the velocity dispersion is still supersonic for the Mach 20 shock. The results presented for the shock tube tests use the higher viscosity parameters, whilst for the sinusoidal potential tests, there is less noise and the standard parameters $\alpha = 1$ and $\beta = 2$ are used. In all cases the higher viscosity parameters had little effect on the velocity dispersions for the clumpy shocks. Alternatively, the velocity dispersion can be determined from the SPH smoothed velocities:

$$\hat{\mathbf{v}}_i = \mathbf{v}_i + \sum_{j \neq i} \frac{m_j}{\rho_j} \mathbf{v}_{ij} \mathbf{W}_{ij}. \quad (2)$$

Since these velocities are smoothed over the neighbouring particles, the velocity dispersion produces less noise. Conse-

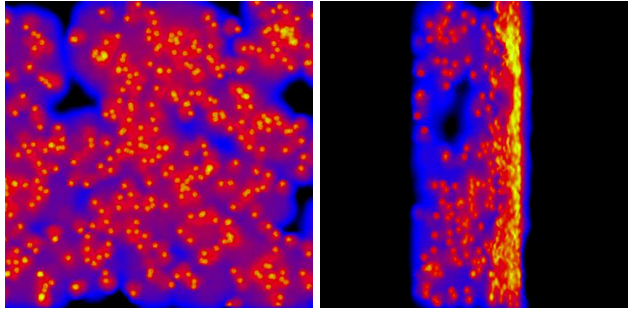


Figure 2. The column density distribution is shown for a shock test where the initial distribution consists of different radii clumps. The gas shocks as it passes through a sinusoidal potential. The left panel ($-1 < x < 1$, $-1 < y < 1$) shows the initial gas distribution ($t=0$) while the right panel ($3.2 < x < 5.2$, $-1 < y < 1$) shows a stage ($t=0.25$) during the shock. The scaling is the same as Fig. 1, and the minimum and maximum of the potential lie at $x = 2$ and $x = 6$.

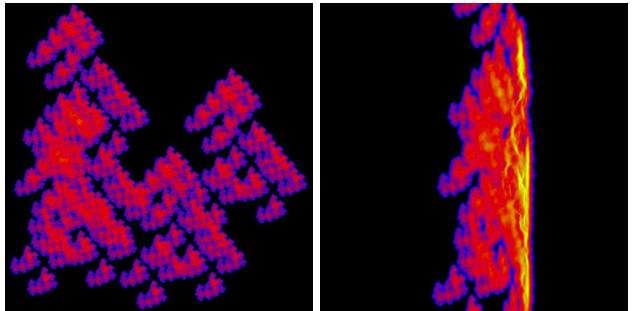


Figure 3. The column density distribution is shown for a shock test where gas distributed according to a 2.2D fractal is passed through a sinusoidal potential. The left panel ($-1.5 < x < 1.5$, $-1.5 < y < 1.5$) shows the initial gas distribution ($t=0$) while the right panel ($3.2 < x < 5.2$, $-1 < y < 1$) shows a stage ($t=0.25$) during the shock. The scaling is the same as Fig. 1.

quently the velocity dispersion is lower (and in all our results subsonic) for the uniform shocks. Except for Fig. 6 though, we use the SPH velocities, since these are the velocities produced by the code.

We plot the velocity dispersion size-scale relation for each of the simulations in Fig. 4, 5, 6, 7 and 8. Also shown is the $\sigma \propto r^{0.5}$ relation, coinciding with most observational results. In Fig. 4 and 5, we show the velocity size-scale relation for uniform and clumpy initial gas distributions, for the shock tube test and the sinusoidal potential. For the sinusoidal potential, the velocity dispersion for the uniform shock dispersion remains flat and subsonic (the sound speed in all simulations is 0.3). This is as expected, since for a uniform shock, the velocity of the shocked gas should have zero velocity dispersion. Again for the shock tube tests, the velocity dispersions for the uniform shocks are relatively flat. By contrast the clumpy shocks show an increasing velocity dispersion with size-scale. The velocity of gas in the shock depends on the amount of mass it has encountered (Section 3.3). For the clumpy shock, gas entering the shock will encounter different amounts of mass (e.g. where gas approaches another clump, or alternatively a relatively empty area) and a range of velocities are exhibited by the shocked

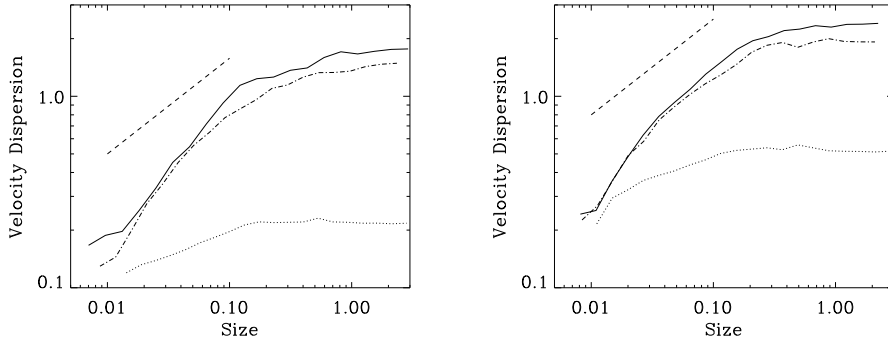


Figure 4. The one-dimensional velocity dispersion of the post-shock gas is plotted against size-scale for the 3D shock tube test. The figures show a $\mathcal{M}=20$ shock (left) and $\mathcal{M}=40$ shock (right). The initial distributions prior to the shock are uniform (dotted line), clumps of radii 0.1 (solid line) and clumps of radii 0.2 (dash-dot line). External pressure boundaries are applied to keep the clumps in equilibrium. The dashed line represents the observed $\sigma \propto r^{0.5}$ relation and the sound speed is 0.3. The initial distribution has a maximum spatial extent of 4, and the viscosity parameters $\alpha = 2$ and $\beta = 4$ are used.

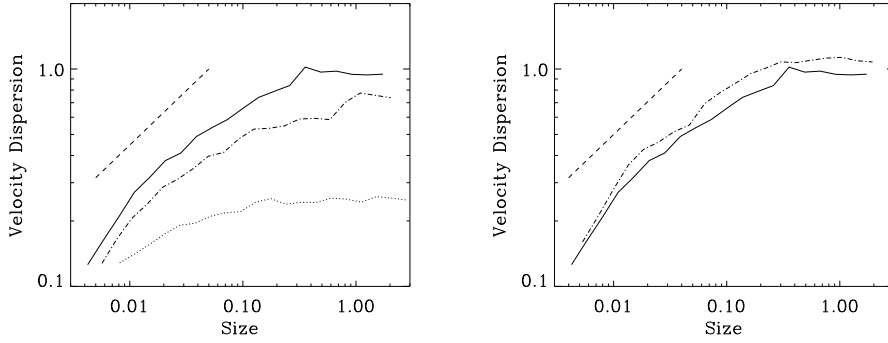


Figure 5. These panels show the one-dimensional velocity dispersion of the post-shock gas plotted against size-scale for the sinusoidal potential. The left panel uses the same initial distributions (with the same key) prior to the shock as Fig. 4, although the maximum initial length scale is 3 for these distributions. The right panel compares the velocity dispersion when external pressure boundaries are applied (solid line) and a diffuse intervening medium is used (dot dash line). For the right panel, the clump radius is 0.1, so these results correspond to the column density images in Fig. 1 (middle and bottom). The dashed line shows $\sigma \propto r^{0.5}$ and the sound speed is 0.3.

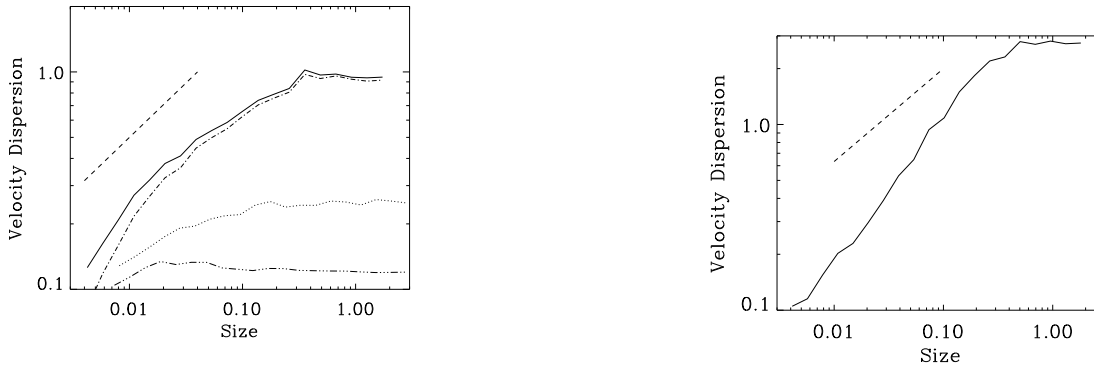


Figure 6. The 1D velocity dispersion relation for is plotted for post-shock gas using the actual and smoothed velocities. The results are shown for the $r=0.1$ clumpy distribution (solid line, actual velocities, dot-dash line, smoothed velocities) and the uniform distribution (dotted line, actual velocities, dot-dot-dash line, smoothed velocities), where the gas passes through the sinusoidal potential. The dashed line shows $\sigma \propto r^{0.5}$ and the sound speed is 0.3.

Figure 7. The 1D velocity dispersion dependence on size-scale is plotted for post-shock gas using an initial distribution of different size clumps. The maximum initial length scale is 3 and the gas shocks when passed through a sinusoidal potential. The dashed line show $\sigma \propto r^{0.5}$ and the sound speed is 0.3.

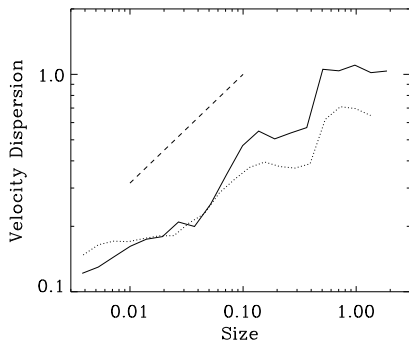


Figure 8. The 1D velocity dispersion dependence on size-scale is plotted for post-shock gas where the initial distributions are a 2.2D (solid) and 2.7 D (dotted) fractal. The gas is passed through a sinusoidal potential and the maximum spatial extent of the initial fractals is 3. The dashed line show $\sigma \propto r^{0.5}$ and the sound speed is 0.3.

gas. This range of velocities increases as the size-scale of the region increases. At some size-scale, the region of gas will contain the full range of structure inherent in the initial distribution. The velocity size-scale relation then remains relatively flat for any further increase in size-scale.

Fig. 5 also compares the velocity dispersion relation when constant pressure boundaries are applied compared to using a diffuse hot medium. The average gradient from the 2 slopes is very similar. Although there is some difference in the form of the velocity dispersion relation, the dynamics appear to be dominated by the cold gas. Fig. 6 compares the velocity dispersion calculated using the actual and smoothed velocities, for a uniform and clumpy shock. Using the smoothed velocities reduces the velocity dispersion in the uniform shock by a factor of around 2. The velocity dispersion is reduced at small scales for the clumpy shock leading to a slight increase in the gradient.

In reality, the ISM has structure on many different length scales. To explore how this affects the resulting velocity dispersion, we have run simulations with a range of clump sizes and with initially fractal distributions. Fig. 7 and 8 also show an increasing velocity size-scale relation for initial gas distributions exhibiting structure on a range of scales. Fig. 7 shows the velocity size-scale dependence where the initial distribution consists of different sized clumps, and Fig. 8 the initial fractal distributions. The velocity dispersion extends to smaller scales due to the presence of structure initially over these scales. Again, using the smoothed velocities slightly increases the gradient of the velocity dispersion against size-scale. The velocity size-scale relation is similar to the observed relation $\sigma \propto r^{0.5}$ for most of the results in Fig. 4, 5, 6, 7 and 8 corresponding to non-uniform initial distributions. The exponent α , where $\sigma \propto r^\alpha$, varies from approximately 0.29 for the 2.7D fractal distribution to 0.75 for the distribution with different clump sizes. With the exception of the $\alpha = 0.75$ result, our results lie within the observed range of values e.g. $\alpha = 0.5 \pm 0.05$ (Solomon et al. 1987; Dame et al. 1986), $\alpha = 0.4 \pm 0.1$, $\alpha = 0.65 \pm 0.08$ (Fuller & Myers 1992), $\alpha = 0.2, 0.5$ (Goodman et al. 1998), representing a range of size scales from cloud cores to molecular clouds.

Generally the distributions with higher filling factors produce shallower gradients in the velocity dispersion relation. As the filling factor increases, the distributions and subsequent velocity dispersions tend towards those of uniform gas, and subsequently the maximum velocity dispersion is less supersonic. The exception appears to be the distribution of different sized clumps, where the velocity size scale relation is somewhat steeper, probably because the filling factor of the smaller clumps is lower, and the smaller clumps contain most of the mass.

3.2 Oblique shocks

Due to the geometry of the shock, the velocity dispersion relations shown in the previous section have only used the v_x component of the velocity. We investigate a more general case by modifying Equation (1) to include a dependence on y . This produces an oblique shock, more similar to spiral shocks. The potential is still sinusoidal, but the minima of the potential now lie in planes inclined by an angle θ to the yz . This is equivalent to an inclination of $90^\circ - \theta$ with the initial flow of the gas. We perform a shock test with this modified potential using the clumpy ($r_{cl}=0.1$) initial distribution. The gas column density for the shock is shown in Fig. 9. The shock is found to induce a velocity dispersion in both v_x and v_y although the v_z dispersion is still subsonic. In Fig. 10, the velocity dispersion is displayed for v_x and v_y , where the shock is inclined at 45° and 30° . The magnitude of the v_x and v_y dispersions is then proportional to the component of the shock front perpendicular to these directions, i.e.

$$\frac{\sigma_x}{\sigma_y} = \frac{\max(|\sigma| \cos \theta, c_s)}{\max(|\sigma| \sin \theta, c_s)} \quad (3)$$

for a given size scale. The term c_s is an estimate of the minimum value of the dispersion, along the line of sight parallel to the shock (though as shown next in Fig. 11, the minimum velocity dispersion in these simulations is slightly lower than c_s).

In Fig. 11, we display the velocity dispersion along the line of sight for different viewing angles, again for the 30° and 45° oblique shocks. The maximum velocity dispersion is chosen at each viewing angle, corresponding to a size scale of ~ 1 (c.f. Fig. 10). The angle ϕ is measured anticlockwise from the $x > 0$ axis, with 10° increments. The peaks then correspond to the line of sight perpendicular to the shock, whilst the minima occur when the line of sight is parallel to the shock. The difference in magnitude of the peaks occurs since the amplitude of the 45° shock is stronger. From these results, we would expect some anisotropy in the magnitude of the velocity dispersion of gas in molecular clouds, corresponding to the geometry of shocks in the gas. For classical models of turbulence, the magnitude of the velocity dispersion is unlikely to show any preferred direction.

3.3 Mass loading

We now examine physically why an increasing velocity size-scale relation emerges in our models. For the clumpy shocks, the gas exhibits a range of densities and velocities across the region of shocked gas. The post-shock velocity of a small parcel of gas depends on the amount of mass it encounters

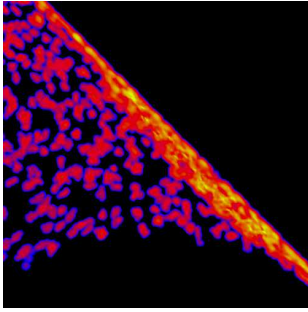


Figure 9. The column density distribution is shown for an oblique shock where the shock front is inclined at 45° to the y axis. The gas initially has a clumpy ($r_{cl}=0.1$) distribution and is passed through a sinusoidal potential. The figure ($2.6 < x < 4.6$, $-0.8 < y < 1.8$) shows a stage ($t=0.2$) during the shock, and the shock in this image lies half way between a potential minimum and the following maximum. The scaling is the same as Figure 1.

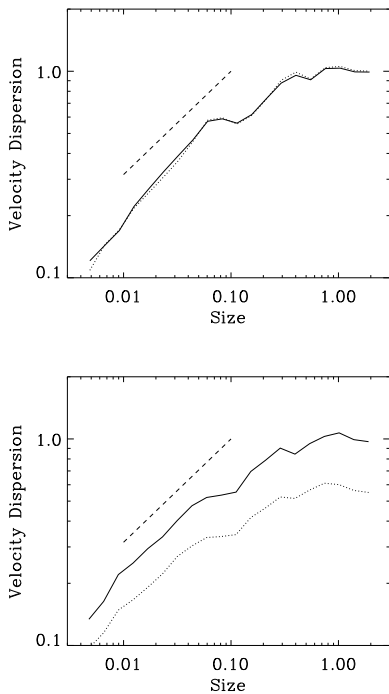


Figure 10. The v_x (solid) and v_y (dotted) velocity dispersions are plotted against size-scale for post-shock gas where the shock is inclined at 45° (top) and 30° (bottom) to the y axis. For $\theta = 45^\circ$, σ_x and σ_y are almost identical. The clumpy ($r_{cl}=0.1$) distribution is used, with a maximum initial length scale of 3. The gas shocks when passed through a sinusoidal potential. The dashed line shows $\sigma \propto r^{0.5}$ and the sound speed is 0.3.

during the shock ('mass loading'). If proportionate amounts of gas enter the shock, conservation of momentum determines that the velocity of the gas in the rest frame of the shock will be small. However, if gas entering the shock encounters only a small amount of material, it's velocity will be less affected and remain of higher magnitude.

Within a region of size-scale less than the structures in the gas, gas in that region will encounter a similar column density in the shock. Therefore the gas will exhibit a low

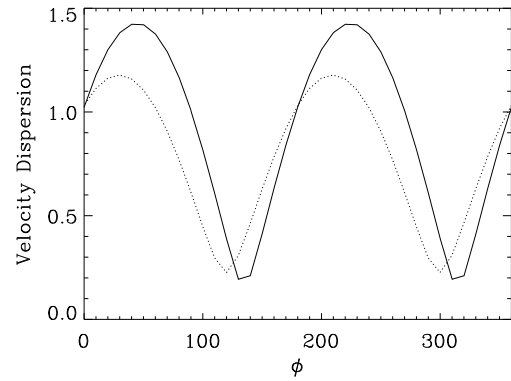


Figure 11. The maximum velocity dispersion along the line sight is plotted against viewing angle ϕ for the 45° (solid) and 30° (dotted) oblique shocks. The angle ϕ is measured anticlockwise from the $x > 0$ axis.

velocity dispersion. However as the size-scale of the region increases, the region will include different structures and gas of different densities. Therefore different parcels of gas will encounter different amounts of mass and exhibit different post-shock velocities. Thus over a larger region a higher velocity dispersion occurs in the gas.

To test the hypothesis of mass loading, we use a semi-analytical approach to calculate the velocity dispersion for the fractal and clumpy distributions. We set up the initial distribution of particles and position a grid across the plane in which the shock will occur, at the centre of the distribution. We then calculate the mass of particles located within a distance l either side of the grid for each grid cell. By applying the conservation of momentum, we determine the expected velocity of the gas in each grid cell, assuming that all the gas within the width l of the centre is compressed into the shock. We took $l=0.2$ for the clumpy shock and $l=0.6$ for the fractal distribution where more of the gas ends up in the shock (this parameter does not change the results providing sufficient material is included to accurately represent the gas distribution). We then calculate the velocity dispersion as described in Section 3.1.

In Fig. 13 we display the velocity size-scale relation for the clumpy distribution (clumps of radius 0.1) and the 2 fractal distributions, from simulations and the corresponding semi-analytical tests. The results for the simulations are all taken from the sinusoidal potential tests. For the clumpy distribution the slope determined from mass loading is somewhat steeper than the results from the simulation. The shape and gradient for the 2.2 D fractal shows a strong correlation between the simulation and the analytical result. For the 2.7D fractal, the semi-analytical velocity dispersion size relation is shallower than that determined by the simulation, although both show a shallower gradient compared to the other 2 distributions. The analytical method can be repeated by setting up distributions with different random seeds to show the degree of scatter in the expected gradients for the distributions. The clumpy shock, which should give very similar distributions regardless of the initial seed, produced a consistent slope of $\alpha = 0.48 \pm 0.03$ compared to $\alpha \approx 0.43$ for the simulation. The fractal distributions

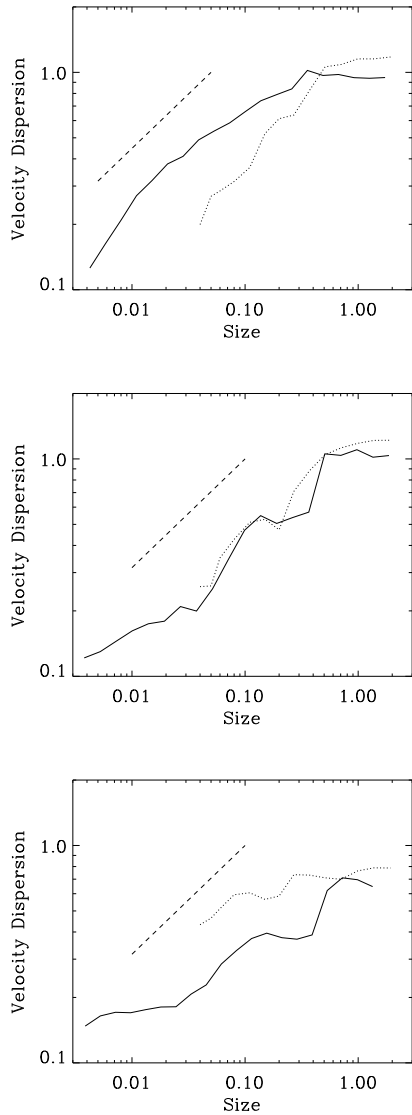


Figure 12. The dependence of the one-dimensional velocity dispersion of the post-shock gas on size-scale is plotted from our simulations (solid) (as in Fig. 5 and 8) and the corresponding semi-analytical result (dotted). The semi-analytical result is calculated assuming the post-shock velocities are dependent on mass loading. Three different distributions are shown: clumpy (clump radii 0.1) (top); 2.2D fractal (middle) and 2.7D fractal (bottom). The dashed line shows $\sigma \propto r^{0.5}$.

showed a much greater variation in slope, the 2.2D fractal giving $\alpha = 0.43 \pm 0.16$ compared to $\alpha \approx 0.4$ for the simulation. For the 2.7D fractal, we found $\alpha = 0.25 \pm 0.15$ for the analytical result, so the line shown on Fig. 12 is at the lowest extent of this range, whilst $\alpha \approx 0.3$ for the simulation.

4 ANALYTICAL MODELS

4.1 Collision of two clumps

The previous results represented plausible mass distributions for the ISM, although consequently we were only able

to calculate the velocity size-scale relation numerically. Here we consider the case of 2 clumps colliding and calculate directly the resulting velocity dispersion. This distribution represents the ‘least uniform’ distribution, so the most removed scenario from a uniform shock. The clumps are assumed to be uniform density spheres and are travelling with equal and opposite velocities. The clumps are offset from each other and so do not collide head on. The parameters describing the collision are shown in Fig. 13, where b is the impact parameter of the 2 clumps. In the following description, we choose a Cartesian axis centred on the point of maximum overlap between the 2 spheres, such that the centre of each sphere is situated at $y = \pm b/2$. In these coordinates, the collision of the clumps is symmetrical about $z = 0$. We take $v_0 = 1$, and the column density is scaled so that maximum column density is $\Sigma_{max} = 1$ along the diameter of each sphere. We first assume that the radii of the clumps are the same, $r_1 = 1$ and $r_2 = 1$.

To calculate the velocity dispersion, we assume that all the gas in the 2 clumps is compressed when they collide. We calculate the post-shock velocity of the material by determining, for each clump, the mass per unit area perpendicular to the shock (Σ_1 and Σ_2 in Fig. 13). The calculation of the velocity dispersion is centred along the column which contains the most mass. In Fig. 13, this corresponds to the column of gas at $y = 0, z = 0$ (i.e. the midpoint of b).

In Fig. 14 we plot the column density for each clump and the post-shock velocity, for a cross-section of the collision along the y axis. By taking a cross-section, the problem is reduced to 1 dimension, and the mass for each sphere can be determined as a function of length scale. Using the idea of mass loading we assume that all gas is compressed into the xy plane. We calculate the expected velocity of gas in the shock by applying the conservation of momentum, i.e.

$$v_s = \frac{(\Sigma_1 - \Sigma_2)v_0}{(\Sigma_1 + \Sigma_2)}. \quad (4)$$

In Fig. 14, $b = 0.5$ and the 2 spheres are overlapping by a distance of 1.5. At $y = 0$ there is an equal contribution in mass from each sphere, and so the velocity in the shock will be 0. The velocity increases to ± 1 for gas which does not encounter any material from the other clump.

We extend this idea to calculate the velocity across a 2D shock from the collision of the clumps. We again assume that the gas is compressed in the yz plane and calculate the mass density entering the shock from each sphere. We then determine the expected post-shock velocity of the gas, again over the yz plane. We calculate the velocity dispersion over a disk centred on the co-ordinates $y = 0, z = 0$. The velocity dispersion is determined over disks of increasing radius, to produce a velocity size-scale relation. We plot the mass-weighted velocity dispersion in Fig. 15, with collisions of different impact parameter.

For the simple case of 2 clumps colliding, the velocity dispersion increases with size scale approximately as a power law, independent of the impact parameter. Increasing the impact parameter transposes the power law to smaller size scales, since the size of the shocked region decreases. For size-scales $> r - b/2$, the velocity dispersion includes gas which does not enter the shock and the velocity size-scale relation flattens. The power law for the shocked gas is somewhat steeper than the $\sigma \propto r^{0.5}$ relation observed, rather

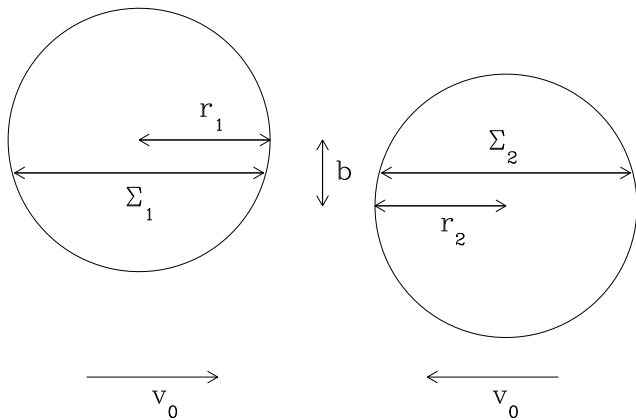


Figure 13. Diagram showing a collision with impact parameter b between 2 spheres. The column densities Σ_1 and Σ_2 perpendicular to the shock are calculated to determine the expected velocity of gas in the shock.

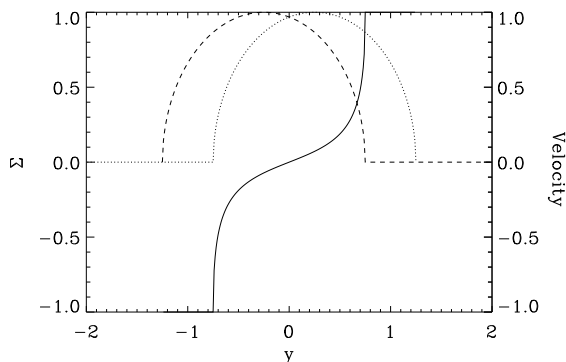


Figure 14. The velocity (solid line) is plotted for a cross-section of post-shock material when 2 spheres collide. The cross-section corresponds to taking a cut where $z = 0$. The dotted and dashed lines show the column density for each sphere along the cross-section.

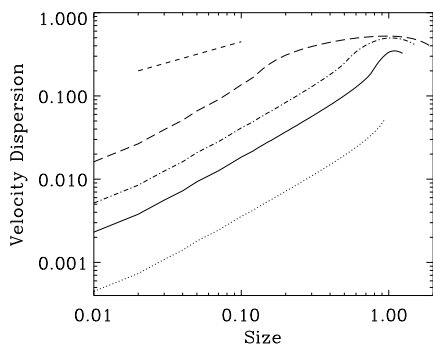


Figure 15. The mass-weighted velocity dispersion predicted for the collision of 2 spherical clumps, each of radii 1 and initially travelling at $v_0 = 1$. The impact parameters of the collision are $b = 0.1$ (dotted), $b = 0.5$ (solid), $b = 1$ (dot-dash) and $b = 1.75$ (long dash) whilst the short dash line represents $\sigma \propto r^{0.5}$.

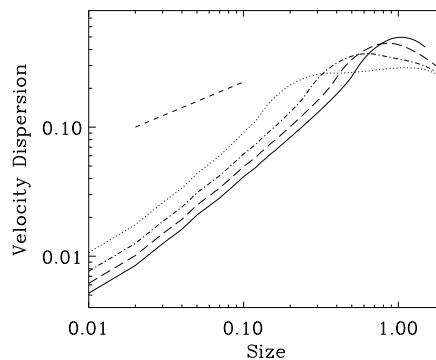


Figure 16. The mass-weighted velocity dispersion predicted for the collision of 2 spherical clumps travelling with initial velocity $v_0 = 1$. The radius of the first clump is set to 1, whilst the radius of the second clump is 1 (solid), 0.75 (long dashed), 0.5 (dot-dash) and 0.25 (dotted). The impact parameter for all the collisions is $b = 1$. The short dash line shows $\sigma \propto r^{0.5}$.

$\sigma \propto r^1$. However, the power law exponent may be expected to decrease when considering larger regions and structure on multiple scales composed of many clumps (Section 4.2).

This power law is also independent of the comparative radii of the 2 spheres. Fig. 16 shows the effect of varying the radius of the second clump (r_2). Similarly to varying the impact parameter, the velocity size-scale relation shifts to smaller scales as r_2 decreases, and levels off at size-scales comparable to r_2 . Scaling both clump radii up or down will extend the velocity size-scale relation to larger or smaller size-scales. For example, if the radius decreases by a factor of 10, the column density and therefore mass-weighted velocity dispersion will also decrease by the same factor.

Assuming that the clumps have velocities $v_0 = 1$, the velocity dispersion for an impact parameter of $b \geq 0.5$ reaches a maximum of ~ 0.3 . Since the initial velocity v can be scaled up or down, the maximum velocity dispersion for an initial velocity of $v_0 c_s$ will be approximately $0.3 v_0 c_s$ (e.g. $3 c_s$ if $\mathcal{M} = 20$). When the impact parameter is small, the velocity dispersion is unlikely to be supersonic (e.g. the maximum is $\sim 0.5 c_s$ when $b = 0.1$ and $\mathcal{M} = 20$). This is expected, since if $b = 0$ the clumps collide head on and the velocity dispersion is 0 everywhere.

4.2 Multiple collisions of clumps

The velocity size-scale relation obtained for 2 clumps colliding is somewhat steeper than those observed for molecular clouds. However this distribution of gas is an extreme case, as in general the gas would be comprised of multiple clumps of various sizes. We now consider many collisions and calculate the average velocity dispersion at each size scale. In all the collisions, we still assume 2 clumps collide, and fix the radius of the first clump to 1. However both the impact parameter b and the second clump radius, r_2 , can be varied. We show 3 different possibilities for the collisions of clumps in Fig. 17. Firstly we vary b randomly, assuming a probability distribution function of $f(b) = 1$, $0 < b < 1$, with r_2 fixed at 1. Secondly, we take b biased toward larger values, so $f(b) = b$, $0 < b < 1$, and r_2 is again fixed at 1. Finally, we

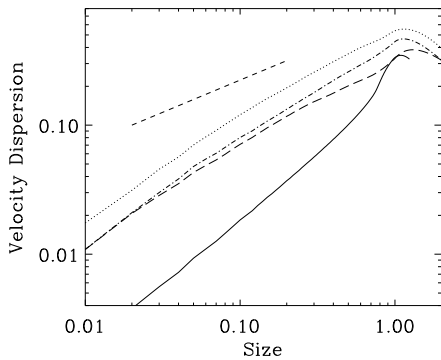


Figure 17. The mass-weighted velocity dispersion predicted for the collision of multiple spherical clumps. The solid line shows the velocity dispersion for 2 clumps of radii 1 and impact parameter 0.5. The dot-dash and dotted lines give the average velocity dispersion for multiple collisions of clumps, where all clumps are assumed to have radii of 1, but the impact parameter varies. The impact parameter is either random (dot-dash) or biased towards large b (dotted). The velocity dispersion for multiple collisions with both random b and r_2 is given by the long dashed line. The short dash line shows $\sigma \propto r^{0.5}$.

allow both b and r_2 to vary randomly, so $f(b) = 1$, $0 < b < 1$ and $f(r_2) = 1$, $0 < r_2 < 1$. For comparison, the velocity size-scale relation from 2 clumps colliding with impact parameter $b = 0.5$ (and both of radii 1) is also included.

The slope is shallower for multiple collisions of random b , giving $\sigma \propto r^{0.8}$. The velocity dispersion was also calculated with b biased towards large values, reflecting the probability of a collision relative to the impact parameter. This produces a slightly flatter slope, although it mainly increases the magnitude of the velocity dispersion. Finally, with both b and r_2 allowed to vary randomly, the gradient decreases further to $\sigma \propto r^{0.7}$.

This is still an incomplete model compared to the simulations of clumpy gas previously described, with further possible variations in the clump and shock geometry. Furthermore, collisions of multiple clumps have not been included, i.e. where > 2 clumps collide simultaneously, or 2 clumps collide with each other before colliding with further material in the shock. The latter is evident in the simulations, where layers of clumps enter the shock and interact with each other. This is again likely to produce a shallower relation compared with the calculations in this section. Overall, for the most structured distribution of 2 offset clumps colliding, the resulting velocity size-scale relation is steep, $\sigma \propto r^1$. For the least structured distribution, i.e. uniform gas, the velocity size-scale relation of the shock is flat. In reality, the distribution of gas, and therefore the gradient of the velocity size-scale relation, is likely to lie within these two extremes.

5 CONCLUSION

We have presented simulations and analysis of shocks for initial distributions of uniform, clumpy and fractal gas. We find an increasing velocity size scale relation in all our results similar to that observed, except for the uniform shocks. For example, for a 2.2 D fractal distribution representative

of the ISM, the velocity size-scale relation is approximately $\sigma \propto r^{0.4}$, in good agreement with observations. The slope of the velocity size-scale relation tends to decrease with distributions corresponding to higher filling factors. The velocity size-scale relations determined for these distributions can be understood in terms of mass loading, as indicated by our analytical tests. Oblique shock tests show that the magnitude of the line-of sight velocity dispersion depends on the angle from which the shock is viewed, providing an observational test for this model.

These results imply that: 1) The observed multi-scale structure of the ISM may explain the velocity dispersion in molecular clouds. This is in contrast to the usual view that turbulence produces the structure of molecular clouds (e.g. Falgarone et al. (2005)); 2) In these models, the dynamics of the shocked gas corresponds to random velocities, rather than classical turbulence, despite the apparent velocity size scaling relation.

ACKNOWLEDGEMENTS

We thank the referee for useful comments and suggestions. Computations included in this paper were performed using the UK Astrophysical Fluids Facility (UKAFF).

REFERENCES

- Ballesteros-Paredes J., Hartmann L., Vázquez-Semadeni E., 1999, *ApJ*, 527, 285
 Benz W., 1990, in in Buchler J.R., ed., *Numerical Modelling of Nonlinear Stellar Pulsations Problems and Prospects Smooth Particle Hydrodynamics - a Review*, Kluwer, Dordrecht. p. 269
 Boldyrev S., 2002, *ApJ*, 569, 841
 Boldyrev S., Nordlund Å., Padoan P., 2002, *ApJ*, 573, 678
 Bonnell I. A., Dobbs C. L., Robitaille T. P., Pringle J. E., 2006, *MNRAS*, 365, 37
 Brunt C. M., 2003, *ApJ*, 583, 280
 Clark P. C., Bonnell I. A., 2006, *MNRAS*, 368, 1787
 Cox D. P., 2005, *ARA&A*, 43, 337
 Dame T. M., Elmegreen B. G., Cohen R. S., Thaddeus P., 1986, *ApJ*, 305, 892
 de Avillez M. A., Breitschwerdt D., 2005, *A&A*, 436, 585
 Dib S., Bell E., Burkert A., 2006, *ApJ*, 638, 797
 Dickey J. M., Lockman F. J., 1990, *ARA&A*, 28, 215
 Dobbs C. L., Bonnell I. A., Pringle J. E., 2006, *MNRAS*, 371, 1663
 Elmegreen B. G., 1997, *ApJ*, 477, 196
 Elmegreen B. G., Falgarone E., 1996, *ApJ*, 471, 816
 Elmegreen B. G., Scalo J., 2004, *ARA&A*, 42, 211
 Falgarone E., Hily-Blant P., Pineau Des Forêts G., 2005, in Wilson A., ed., *The Dusty and Molecular Universe: A Prelude to Herschel and ALMA The multiphase and multiscale diffuse interstellar medium*, Paris. pp 75–80
 Falgarone E., Phillips T. G., 1990, *ApJ*, 359, 344
 Fuller G. A., Myers P. C., 1992, *ApJ*, 384, 523
 Goodman A. A., Barranco J. A., Wilner D. J., Heyer M. H., 1998, *ApJ*, 504, 223
 Hayashi M., Kobayashi H., Hasegawa T., 1989, *ApJ*, 340, 298

- Heitsch F., Burkert A., Hartmann L. W., Slyz A. D., Devriendt J. E. G., 2005, *ApJL*, 633, L113
Heyer M. H., Brunt C. M., 2004, *ApJL*, 615, L45
Klessen R. S., 2001, *ApJ*, 556, 837
Koda J., Sawada T., Hasegawa T., Scoville N. Z., 2006, *ApJ*, 638, 191
Kornreich P., Scalo J., 2000, *ApJ*, 531, 366
Larson R. B., 1981, *MNRAS*, 194, 809
Mac Low M.-M., Klessen R. S., 2004, *Reviews of Modern Physics*, 76, 125
Monaghan J. J., 1992, *ARA&A*, 30, 543
Monaghan J. J., Lattanzio J. C., 1985, *A&A*, 149, 135
Myers P. C., 1983, *ApJ*, 270, 105
Ossenkopf V., Mac Low M.-M., 2002, *A&A*, 390, 307
Passot T., Pouquet A., Woodward P., 1988, *A&A*, 197, 228
Perault M., Falgarone E., Puget J. L., 1985, *A&A*, 152, 371
Piontek R. A., Ostriker E. C., 2005, *ApJ*, 629, 849
Scalo J., Vazquez-Semadeni E., Chappell D., Passot T., 1998, *ApJ*, 504, 835
Sellwood J. A., Balbus S. A., 1999, *ApJ*, 511, 660
She Z.-S., Leveque E., 1994, *Physical Review Letters*, 72, 336
Solomon P. M., Rivolo A. R., Barrett J., Yahil A., 1987, *ApJ*, 319, 730
Wada K., Meurer G., Norman C. A., 2002, *ApJ*, 577, 197
Wada K., Norman C. A., 2001, *ApJ*, 547, 172
Zhang X., Lee Y., Bolatto A., Stark A. A., 2001, *ApJ*, 553, 274

This paper has been typeset from a \TeX / \LaTeX file prepared by the author.